Linking Equatorial African precipitation to Kelvin wave processes in the CP4-Africa convection-permitting regional climate simulation

Article

Accepted Version

Journal of the Atmospheric Sciences

Linking Equatorial African precipitation to Kelvin wave processes in the CP4-Africa convection-permitting regional climate simulation

--Manuscript Draft--

Manuscript Number:	JAS-D-21-0039
Full Title:	Linking Equatorial African precipitation to Kelvin wave processes in the CP4-Africa convection-permitting regional climate simulation
Article Type:	Article
Corresponding Author:	Godwin Ayesiga University of Reading Reading, UNITED KINGDOM
Corresponding Author's Institution:	University of Reading
First Author:	Godwin Ayesiga
Order of Authors:	Godwin Ayesiga
	Christopher E. Holloway
	Charles JR. Williams
	Gui-Ying Yang
	Rachel Stratton
	Malcolm Roberts
Abstract:	Observational studies have shown the link between Convectively Coupled Kelvin Waves (CCKWs) and eastward propagating rainfall anomalies. We explore the mechanisms in which CCKWs modulate the propagation of precipitation from west to east over Equatorial Africa. We examine a multi-year state-of-the-art Africa-wide climate simulation from a convection permitting model (CP4A) along with a parameterised global driving-model simulation (G25) and evaluate both against observations (TRMM) and ERA-Interim (ERA-I), with a focus on precipitation and Kelvin wave activity. We show that the two important related processes through which CCKWs influence the propagation of convection and precipitation from west to east across Equatorial Africa are: 1) low-level westerly anomalies that lead to increased low-level convergence, and 2) westerly moisture flux anomalies that amplify the lower-to-mid-tropospheric specific humidity. We identify Kelvin wave activity using zonal wind and geopotential height. Using lagged composite analysis, we show that modelled precipitation over Equatorial Africa can capture the eastward propagating precipitation signal that is associated with CCKWs. Composite analysis on strong (high-amplitude) CCKWs shows that both CP4A and G25 capture the connection between the eastward propagating precipitation anomalies and CCKWs. In comparison to TRMM, however, the precipitation signal is weaker in G25, while CP4A has a more realistic signal. Results show that both CP4A and G25 generally simulate the key horizontal structure of CCKWs, with anomalous low-level westerlies in phase with positive precipitation anomalies. These findings suggest that for operational forecasting, it is important to monitor the day-to-day Kelvin wave activity across Equatorial Africa.

Linking Equatorial African precipitation to Kelvin wave processes in the CP4-Africa convection-permitting regional climate simulation

Godwin Ayesiga *

Department of Meteorology, University of Reading, Reading, United Kingdom

Christopher E. Holloway

Department of Meteorology, University of Reading, Reading, United Kingdom

Charles JR. Williams

School of Geographical Sciences, University of Bristol, Bristol, United Kingdom

Gui-Ying Yang

National Centre for Atmospheric Sciences and Department of Meteorology, University of Reading, Reading, United Kingdom

Rachel Stratton

Met Office, Exter, United Kingdom

Malcolm Roberts

Met Office, Exter, United Kingdom

Corresponding author: Godwin Ayesiga, g.ayesiga@pgr.reading.ac.uk

ABSTRACT

Observational studies have shown the link between Convectively Coupled Kelvin Waves (CCKWs) and eastward propagating rainfall anomalies. We explore the mechanisms in which CCKWs modulate the propagation of precipitation from west to east over Equatorial Africa. We examine a multi-year state-of-the-art Africa-wide climate simulation from a convection permitting model (CP4A) along with a parameterised global driving-model simulation (G25) and evaluate both against observations (TRMM) and ERA-Interim (ERA-I), with a focus on precipitation and Kelvin wave activity. We show that the two important related processes through which CCKWs influence the propagation of convection and precipitation from west to east across Equatorial Africa are: 1) low-level westerly wind anomalies that lead to increased low-level convergence, and 2) westerly moisture flux anomalies that amplify the lower-to-mid-tropospheric specific humidity. We identify Kelvin wave activity using zonal wind and geopotential height. Using lagged composite analysis, we show that modelled precipitation over Equatorial Africa can capture the eastward propagating precipitation signal that is associated with CCKWs. Composite analysis on strong (high-amplitude) CCKWs shows that both CP4A and G25 capture the connection between the eastward propagating precipitation anomalies and CCKWs. In comparison to TRMM, however, the precipitation signal is weaker in G25, while CP4A has a more realistic signal. Results show that both CP4A and G25 generally simulate the key horizontal structure of CCKWs, with anomalous low-level westerlies in phase with positive precipitation anomalies. These findings suggest that for operational forecasting, it is important to monitor the day-to-day Kelvin wave activity across Equatorial Africa.

1. Introduction

Variations in the frequency, spatial distribution and intensity of precipitation over Equatorial Africa (15^{o}S - 15^{o}N, 0 - 51^{o}E) threaten millions of lives that depend on rainfall for a decent livelihood (e.g., FAO 2016). Equatorial Africa is a large area that spans different seasons and different precipitation patterns (Nicholson and Dezfuli 2013a;Nicholson 2017). A thorough understanding of these variations and their drivers across spatial and temporal scales is a positive step toward improving the precipitation forecasts. Synoptic-scale precipitation variability over Equatorial Africa is largely modulated by large-scale features (e.g., Schlueter 2020). For example, in their analysis of daily precipitation in both boreal spring and autumn, Ayesiga et al. (2021) found that Convectively Coupled Kelvin Waves (CCKWs) play a role in the eastward propagation of enhanced precipitation across Equatorial Africa.

In Equatorial Africa, much of the rains within 5^o about the equator occurs in boreal spring and autumn and has been associated with convective activity during the north-south progression of the tropical rain-belt (e.g., Nguyen and Duvel 2008). Within each season, rainfall varies considerably in space and time, making forecasting a challenge. Skillful forecasts of precipitation episodes associated with synoptic spatial-and temporal-scale features such as CCKWs are hampered by several factors such as incomplete understanding of the role of these modes of variability in influencing precipitation as well as their interaction with localised convective features (e.g., Dezfuli et al. 2015). For example, the role of CCKWs in influencing precipitation over Equatorial Africa is insufficiently studied. In this study, we examine the processes through which CCKWs influence the eastward propagation of precipitation across Equatorial Africa. Also, we assess whether the eastward propagating precipitation signal seen in observations is present in modelled precipitation. Additionally, we investigate how well the processes through which CCKWs modulate west-east

progagation of precipitation are captured in a high-resolution convection permitting model and a convection parameterised global model.

Tropical precipitation is often associated with tropical disturbances such as equatorial waves (CCKWs, Rossby waves, Mixed Rossby Gravity waves etc) that organise convective activity (e.g., Kiladis et al. 2009). For example, Nakazawa (1988) identified eastward moving super cloud clusters composed of individual westward moving mesoscale systems over the western Pacific. Nakazawa (1988) reasoned that the eastward propagation of the super cloud cluster is sustained through development of low-level convergence and convective cells east of a mature-stage cloud cluster, and suggested that both Kelvin and Rossby waves were important in these super clusters. Over tropical Africa, CCKWs are most prevalent in boreal spring (e.g., Huang and Huang 2011). CCKWs generally slow down in proportion to their degree of convective coupling, but they have been estimated to travel through equatorial Africa at 12 - 15 m s^{-1} (e.g., Mekonnen et al. 2008; Laing et al. 2011). CCKWs also play a role in the link between precipitation in western and eastern equatorial Africa (e.g., Mekonnen and Thorncroft 2016; Ayesiga et al. 2021). Some publications such as Straub and Kiladis (2002), Nguyen and Duvel (2008) and Guo et al. (2014) have noted that as CCKWs propagate eastward, they influence the local convective systems.

Several observational and modelling studies have explored the influence of CCKWs on convection and precipitation during West Africa's monsoon (e.g., Mounier et al. 2007; Mekonnen et al. 2008; Schlueter et al. 2019a) while other publications focused on ocean basins where the signal of equatorial waves is strong (e.g., Wheeler et al. 2000). Detailed examination of the observed and modelled dynamics involved in the coupling between CCKWs and precipitation over Equatorial Africa are uncommon. In addition, much of the knowledge on Kelvin wave activity over Equatorial Africa is based on filtering of Outgoing Longwave Radiation (OLR) in a zonal wavenumber-

frequency domain confined by the dispersion curves of Kelvin waves. The current study identifies Kelvin wave activity based on dynamical fields and uses precipitation as a proxy to convection.

Nevertheless, there are some publications that have studied Kelvin waves (both wet and dry phase) over some regions in Africa or Africa as a whole (e.g., Nguyen and Duvel 2008; Jackson et al. 2019; Schlueter et al. 2019). The conclusions from these studies are diverse but all echo the importance of CCKWs for synoptic-scale precipitation variability. In Congo basin, Nguyen and Duvel (2008) found Kelvin wave structure in the horizontal wind field that resembled the theoretical Kelvin waves. The convective signal associated with CCKWs was characterised with a period of 3-6 days. They also highlighted that the convective signal associated with CCKWs tends to weaken as the waves propagate over highlands on the western branch of the East African Rift Valley. Jackson et al. (2019) attributed about 15% of variance in daily mean precipitation during April over some areas in Eastern Equatorial Africa (EEA; 15^{o}S-15^{o}N, 29-51^{o}E) to CCKWs. A case study in Mekonnen et al. (2008) showed that passage of a CCKW was associated with increased precipitation in comparison to the days preceding the passage of the wave and Ayesiga et al. (2021) showed precipitation anomalies of up to 5 mm day^{-1} associated with CCKWs. A thorough understanding of how CCKWs modulate the west-east intra-equatorial Africa precipitation connection is an important step toward exploiting the potential source of precipitation predictability.

From a modelling perspective, Huang et al. (2013) investigated the representation of equatorial waves in Coupled Model Intercomparision Project phase 3 (CMIP3) models and found that only 20% of the models evaluated simulated a realistic seasonal cycle of Kelvin wave activity. Results in Straub et al. (2010) showed that 75% of the 20 CMIP3 model simulations failed to reasonably represent CCKWs and that most models exhibited deficiencies in capturing the lower tropospheric humidity signal. Yang et al. (2009) evaluated the representation of equatorial waves in the Hadley Centre Atmospheric Model, version 3 (HadAM3) and the New Hadley Centre Atmospheric Model,

version 1 (HadGAM1) against ERA-15 and satellite data and concluded that both models had inadequacies in capturing the coupling between these waves particularly CCKWs' and convection. The findings from investigations related to the representation of equatorial waves in CMIP3 models (e.g., Straub et al. 2010; Huang et al. 2013) and phase 5 (CMIP5) simulations (e.g., Wang and Li 2017) suggest that in general, global models struggle to produce horizontal and vertical structure that resembles observed CCKWs. Recent studies have indicated that the parameterised coarse resolution in Atmospheric General Circulation Models (AGCMs) limits their ability to capture the interaction between equatorial waves and the precipitation. In addition, AGCMs depend on convection parameterization schemes which generally lack robust dynamics-convection coupling. Comparison of model output from coarse-resolution models with parameterised convection with observations and convection permitting model output is likely to lead to improvements in the coarse-resolution models.

Cloud-resolving regional climate model runs have been used to improve our understanding of wave-convection coupling (e.g., Tulich and Mapes 2008; Tulich et al. 2011). In the current study, a regional convection permitting simulation (CP4A) and its driving global simulation (in which convection is parameterised) are analysed. While Jackson et al. (2019) investigated the response of precipitation to CCKWs in both CP4A and the global simulation analysed here, they used continent-wide observed and modelled Outgoing Longwave Radiation (OLR) as a proxy to convection, and focused on April only. In the present study, Kelvin wave activity is obtained from equatorial wave analysis based on dynamical fields (zonal and meriodional wind) and geopotential height, and the focus is on Equatorial Africa for the whole March-April-May (MAM) rainy season.

Kelvin waves have been found to modulate extreme precipitation in Asia (e.g., Ferrett et al. 2020; Baranowski et al. 2020). Wheeler and Nguyen (2015) pointed out that through monitoring African Kelvin waves, convective rainfall events can be predicted several days before occurrence.

Recent work in Yang et al. (2021) suggested that recent numerical weather prediction models have some skill in predicting Kelvin waves. Despite the role of CCKWs in influencing Equatorial Africa's convection and precipitation (e.g., Nguyen and Duvel 2008; Laing et al. 2011; Mekonnen and Thorncroft 2016), the mechanisms through which CCKWs connect precipitation in Western Equatorial Africa (WEA; 15^{o}S-15^{o}N, 0-29^{o}) to that in EEA remain largely unclear. For example, what are the major structures of circulation anomalies associated with the interaction between CCKWs and the eastward propagating precipitation anomalies over Equatorial Africa? How does the interaction between the eastward propagating CCKWs and the moisture field evolve in space and time across Equatorial Africa? And, how well are these interactions captured in high-resolution convection permitting climate models?

This study aims at shedding light on the interaction between synoptic timescale convective precipitation and CCKW dynamics over Equatorial Africa. More precisely, we aim at improving our knowledge of the association between the eastward propagating precipitation signal found in Ayesiga et al. (2021) and CCKWs by examining a high resolution simulation from a Convection Permitting (CP) Regional Climate Model (RCM), coarse global model simulation, observations (TRMM) and Reanalysis (ERA-I). In the next section, we describe the data sets and methods used in this study. The results are shown in section 3. In section 4, a discussion and conclusions are presented.

2. Observations, Simulations and Methods

a. Observations

The Tropical Rainfall Measuring Mission (TRMM) Multi-satellite Precipitation Analysis (TMPA) precipitation product is a multi-satellite data set produced from a combination of infra-red

rainfall estimates from geosynchronous satellites and the passive microwave rainfall information from the TRMM Microwave Imager (a multi-channel passive microwave radiometer) (Huffman et al. 2007). This dataset has a spatial resolution of 0.25^{o}x 0.25^{o}, a 3-hourly temporal resolution and is available for a period 1998-2019. The present study uses 3B42 version 7 daily TRMM estimates for a period 1998-2007.

b. Reanalysis

ERA-Interim (ERA-I) data from the European Centre for Medium-Range Weather Forecasts (ECMWF) is used for wind field, specific humidity and potential temperature. ERA-I is a global reanalysis produced with ECMWF's Integrated Forecast System (IFS) (e.g., Dee et al. 2011) and spans 1 January 1979 - 31 August 2019. This data was output at a spatial resolution of ~0.7^{o}x 0.7^{o}, 6-hourly temporal resolution and 37 vertical levels. While ERA-I will contain biases and uncertainties related to its model components (particularly the convection parametrisation) as well observational uncertainty, we rely on it as our estimate of observational "truth" with respect to equatorial waves and their environment, since these large-scale fields should be relatively well constrained. Because large-scale winds are influenced by observed wind fields (e.g., during data assimilation), it is expected that they will be better resolved than erratic fields such as precipitation (e.g., James et al., 2018). ERA-I is one of the reanalysis datasets that have been widely used to diagnose large circulation features over Equatorial Africa (e.g., see Mekonnen and Thorncroft, 2016; Zebaze et al., 2017; Nicholson 2018, Jackson et al., 2019). In addition, prior to the current study, the third co-author generated an equatorial wave dataset based on ERA-I. This dataset was used here to calculate the Kelvin wave-induced divergence field. It would therefore be expected that the dynamical fields from ERA-I would be appropriate for the present study. A 9 year period (1998-2006) is used in this study.

c. Model simulations

This study examines two climate model simulations: a) A convection permitting regional climate simulation (CP4A), and b) the N512L85-resolution global model climate simulation. The global model simulation examined in this study is from a prototype version of the Global Atmosphere/Land (GA 7.0/GL7.0) configuration of the Met Office Unified Model (UM) (e.g.,Walters et al.,2019b). This is free-running standard parameterised convection global atmospheric model. For consistency with Jackson et al. (2019), we refer to this simulation as "G25". This model is one of the configurations of the Met Office Unified Model (UM). The UM uses a convection scheme based on Gregory and Rowntree (1990) with a number of extensions to include down-drafts and convective momentum transport. The G25 was run with 85 vertical levels up to 85km and approximately 26km and 39km grid spacing in latitudinal and longitudinal direction respectively. The model used a deep convection scheme that differs from the original Gregory and Rowntree (1990) in using a Convective Available Potential Energy (CAPE) closure based on Fritsch and Chappell (1980) and a shallow convection scheme based on Grant (2001). The shallow convection scheme has larger entrainment rates than the deep convection scheme and allows a match with shallow convection in a cloud-resolving model (Walters et al. 2019b). G25 was forced with Sea Surface Temperatures (SSTs) obtained from the Reynolds dataset of the daily high-resolution blended analyses for SST, and the Global sea-Ice and Sea Surface Temperature (GISST) climatology was used for the Lake Victoria SSTs (Stratton et al. 2018). This simulation is available for a period 1988-2010, however, this study uses data for 1998-2006.

The CP4A is a free-running decade long (1997 - 2006) simulation from a convection permitting UM run over an Africa-wide domain (Stratton et al. 2018). The G25 described above was used to supply the 3-hourly lateral boundary conditions to CP4A. The lateral boundary conditions were

updated at a 3-hour frequency. This simulation was run over a domain apprimately 45.525°S-39.505°N, 24.5°W-56.48°E. The SSTs used to force CP4A are the same as those used in G25; however over Lake Victoria in CP4A, the monthly nighttime climatological lake temperature from the Lake Surface Water Temperature and Ice Cover (ARC-Lake) was used. Additionally, the fields (except the soil moisture) from G25 for 1 January 1997 were used as the atmospheric initial conditions for the CP4A. The climatological data with a resolution of 50km from an offline Joint UK Land Environment Simulator (JULES) land surface simulation was used to initialise the soil moisture. CP4A was run mostly with a time step of 100 s and has hourly output frequency, but the current study analyses daily mean of the various fields. CP4A has a spatial resolution of approximately 4.5 km at the equator and 80 vertical levels up to 38.5 km. Because precipitation in this region is produced by convective systems, CP4A provides a virtual laboratory to better understand convection-dynamics interactions, thereby improve the representation of the coupling between convection and Kelvin waves in models. It is worth noting that while the CP4A has stochastic perturbations to the boundary layer, G25 does not have such perturbations.

There are several differences in the model setup between CP4A and G25. For example, in CP4A, convection is explicitly represented but G25 implements a convection scheme. Also, CP4A's large-scale cloud scheme is based on Smith (1990) but G25 implements a prognostic cloud scheme as described in Wilson et al. (2008). More differences can be found in (Stratton et al. 2018).

Another RCM was run over a similar domain as CP4A but with ~25km grid spacing and parameterised convection (P25; Stratton et al.,2018). Following a proposition in Frierson (2007) that the representation of equatorial waves in climate models is constrained partly by the convection scheme, we also wanted to explore how the horizontal and vertical structure of CCKWs in a convection permitting model compares with that in a convection parameterised model. We chose

to examine G25 instead of P25 because G25 has data over the entire tropics, allowing for reliable identification of equatorial waves.

Jackson et al. (2019) identified a CCKWs signal in CP4A data that was coarse grained to approximately 1.5^{o}. Nguyen and Duvel (2008) analysed OLR at 2.5^{o} and identified a Kelvin wave signal over Equatorial Africa. We expect that the 1^{o} x 1^{o} resolution used in the present study is sufficient for our purpose.

d. Methods

1) Anomalies and Empirical Orthogonal Teleconnection Analysis (EOT)

The observed and simulated daily precipitation anomalies were subjected to an Empirical Orthogonal Teleconnection Analysis (EOT) algorithm to identify sub-regions of similar daily precipitation variability. The anomalies were calculated by subtracting a 30-day running mean of the daily 9 year precipitation climatology from each year to remove the annual cycle and this was followed by subtracting the 100-day running mean from the time series at every grid point. The subtraction of the 100-day moving average was undertaken to remove signals of low-frequency modes of climate variability. Linear regression technique is then used to remove signals of long-term trend and the remaining residual is subjected to the EOT algorithm. It starts with identifying a grid point whose time series best matches the domain-area-average time series. This point may be referred to as the "base-point". The second step involves computing the correlation between the base-point time series and every grid point time series in the domain. In the third step, a sub-region is defined by identifying the latitude-longitude box demarcated by the meridional and zonal line segments intersecting the base point and including all contiguous gridpoints along the segments whose correlation coefficient is between the base point and the gridpoint time series exceed 0.2 (This step is only needed for our purposes here and may not be useful for a general EOT analysis.) After

identifying a sub-region, a fourth step involves subtracting the variance explained by the base point from every gridpoint in the domain. This creates a "new" time series at every gridpoint. The four steps are repeated to identify other sub-regions implying that in each iteration, a sub-region is identified. One limitation in this study is that the sub-regions from each simulation were identified independently from the observations (TRMM). The details on how the EOT approach was used for obtaining sub-regions of similar daily precipitation variability can be obtained in Ayesiga et al. (2021). In this study, a resolution of 0.25^{o}x $0.25^{o}$is used for all the datasets in identification of the sub-regions and correlation coefficient analysis however, for other analyses, anomalies on 1^{o}x $1^{o}$are used. The results from analysis of CP4A precipitation on its native spatial resolution show precipitation that is too intense because the model underestimates and overestimates low and high precipitation rates respectively (Berthou et al. 2019). When the precipitation field is coarse grained to 25 km x 25 km, the precipitation field matches well with the observations (Berthou et al. 2019). The sub-regions identified are used as reference sub-regions for computing time lagged correlation coefficients and composites as described below.

2) Equatorial Wave data

Several studies identified CCKWs over Africa by undertaking spectral analysis of OLR (e.g., Jackson et al., 2019; Mekonnen and Thorncroft, 2016). However, using OLR to identify equatorial waves has two potential limitations. First, using filters in the zonal wavenumber-frequency domain to partition "wave modes" can be susceptible to errors induced by changes in wave frequency due to Doppler shifting by the background flow or effects of shear. Second, the reliance on identifying the OLR signal can lead to the failure to identify equatorial modes in regions which may not be convectively active, and because they are identified from an OLR signal they cannot easily be used to relate the precipitation signal to the wave structure independently, and are not able to

characterize the relationship between convection and the wind structures within waves. Yang et al. (2003) developed a less constraining method for identifying equatorial waves. It does not assume that the linear adiabatic theory for equatorial waves on a resting atmosphere is directly applicable. In particular, the dispersion relation and vertical structure are not imposed, and because of using a broad-band filter the method is not limited to a prescribed narrow space-time spectral filter and can account for Doppler shifts automatically. Potential equatorial waves are identified by projecting the dynamical fields in the tropics at each pressure level onto a set of horizontal structure basic functions described by parabolic cylinder functions. Another advantage of this method is that the equatorial wave winds can be used to investigate the connection and interaction of dynamical fields (e.g., wave divergence) and convection. Here, we isolate Kelvin waves we used this method over Spectral analysis. It is important to note that before projecting the fields onto the equatorial wave modes, the annual cycle is removed and then the data is filtered using a specified spectral domain to separate it into the eastward-and westward-propagation components. Yang et al. (2003) provides further details including the equations used to undertake the projection. To identify Kelvin waves in the model simulations, we apply their approach to both simulations and ERA-I as in Ayesiga et al. (2021).

The isolation of equatorially trapped waves is best achieved using a zonally complete tropical domain, and so most studies have examined data from global observations or simulations. To detect Kelvin waves in CP4A, we start by regenerating a "new" global dataset that is comprised of both CP4A and G25. This is done by cutting out the African domain from G25 and replacing it with the CP4A. Both simulations are coarse grained to a uniform grid before stitching them together. The sharp contrast at the longitudes (~24^{o}W and 56^{o}E) at which the joining is undertaken is smoothed by running a 5-point moving average along each latitude. The stitching is done for the sole purpose of creating an equatorial wave dataset and for all subsequent analysis, we use the CP4A's fields.

The resulting equatorial wave data at say 850 hPa is a wave's wind data at spatial resolution of 1^{o}x 1^{o} on a daily time scale for a period 1998-2006. However, due to set up problems, CP4A's geopotential height and dynamical fields for the first 6 months of 1997 were not archived and so, year 1997 was excluded in the subsequent analysis. The methodology used here to identify Kelvin wave activity has been successfully applied in a wide range of studies to investigate CCKWs both in observations (Yang et al., 2007a) and model evaluation (Yang et al. 2009), including the vertical propagation of equatorial waves in different phases of QBO (Yang et al., 2011, 2012), the influence of ENSO on equatorial waves and tropical convection (Yang and Hoskins, 2013, 2016), the connection between African easterly wave and equatorial waves (Yang et al. 2018), and the relationship between precipitation and equatorial waves in Southeast Asia (Ferrett et al. 2020).

3) Composite Analysis and Statistical Significance Testing

The composite technique is used here because it provides a general view of several individual events. To develop an index by identifying all the days with a high amplitude CCKW activity, we first calculate an area averaged time series of the Kelvin wave convergence along the central latitude but between two longitudes that define a sub-region in WEA (see green box in each panel in top row of Figure 1). Then, high-amplitude Kelvin wave events are defined as days on which the Kelvin wave convergence amplitude exceeded the 90^{th} percentile of Kelvin wave convergence (below the 10^{th} percentile of the divergence) over the sub-region. Wheeler and Nguyen (2015, their Fig.7) used a box that has approximately the same dimensions as those used in the present study to demonstrate the propagation of a Kelvin wave signal across Africa. In this study, we use the term wave "Kelvin wave convergence" to refer to lower-level convergence of the Kelvin wave wind field in the equatorial wave dataset.

We construct a composite by taking an average over the days identified. We assume that the individual Kelvin wave events have reasonably similar propagation characteristics. Our interest is to gain a picture of how an average Kelvin wave event influences precipitation across Equatorial Africa. For composites of various fields on a high-amplitude Kelvin wave events, "day 0" is when the Kelvin wave amplitude exceeds the threshold in a sub-region in WEA (see green box in Figure 1). Note that some Kelvin wave events neighbour other events in time. Out of the 103 Kelvin wave events used in the composites, about 46% are isolated in time from other events, 33% occur on days that are directly preceded or followed by days that are also Kelvin wave events, and 18% occur in clusters of three consecutive days that are all Kelvin wave events. Wheeler and Nguyen (2015, their Fig.7) used 114 events to demonstrate the propagation of the Kelvin wave signal, suggesting that the number of Kelvin wave events used here is sufficient. The statistical significance of the anomalous fields and correlation coefficients was undertaken using a non-parametric bootstrapping technique that involves taking 1000 random samples. For correlation coefficients, sampling is done by randomly drawing with replacement of blocks of 100 days, and then, stitching them together to conserve the size of the time series. By sub-dividing the time series into blocks of 100 days, we retain the synoptic-timescale autocorrelation of the sampled time series. In computing the statistical significance, the null hypothesis is that the test statistic is not significantly different from zero and a 95% confidence level is applied. In essence, a given correlation coefficient was considered statistically significant if its absolute value was greater than the absolute value of 95% of the correlation coefficients calculated using the random samples. Unless stated, the anomalies used in correlation coefficient analysis and compositing are calculated as described above.

To examine the extent to which Kelvin wave events are linked to precipitation events, another index that is based on precipitation over a pair of sub-regions is developed. Before computing the threshold, dry days (the days in the raw precipitation where the amount is less than 0.1 mm day^{-1}

) are removed from the time series. For each sub-region, the 66.7^{th} percentile of the anomalous area averaged time series over a sub-region is chosen as a threshold, implying that the threshold is sub-region dependent. Because operational precipitation forecasting systems tend to identify heavy precipitation using the 66.7^{th} percentile, we adopt it here to identify precipitation events. As was done in Ayesiga et al. (2021), a precipitation event is one that satisfies two conditions. First, precipitation occurs in excess of a threshold in a sub-region in WEA. And then, two days later, the precipitation in the corresponding sub-region in EEA exceeds that sub-region's threshold given that the previous day's precipitation was below the threshold. In this study, the precipitation events for each dataset are identified using a pair of sub-regions shown in the top row of Figure 1. This pair of sub-regions was found to better reveal the WEA-EEA precipitation connection; further details on this and the definition of a precipitation event can be found in Ayesiga et al. (2021). In the current study, a pair of sub-regions shown in the top row of Figure 1 is used to identify precipitation events in each dataset.

3. Results

a. Sub-region identification and the eastward propagating signal in observed and simulated precipitation

Results from subjecting the 9 year daily precipitation anomalies from TRMM and both simulations to an EOT algorithm show that while there are differences in the location of the sub-regions identified by TRMM and the modelled precipitation based sub-regions, there were several overlaps (figure not shown). For example, both CP4A and G25 identified a sub-region contained within 9^oS-3^oS, 16^oE-21^oE and also 4^oS-2^oN, 31^oE-36^oE (see Figure 1). These sub-regions are in correspondence with W9 and E3 in Ayesiga et al. (2021) (their Figure 1). As an example, a pair

(green for WEA and brown for EEA) of sub-regions identified by an EOT algorithm is shown in top panels of Figure 1. Ayesiga et al. (2021) used 16 years of observed daily precipitation anomalies and identified 17 and 8 sub-regions of similar daily precipitation characteristics in WEA and EEA respectively (their Figure 1). They calculated correlation coefficients for each sub-region in WEA with every sub-region in EEA and identified a sub-region in WEA (7^oS-3^oS, 16^o-21^oE), that indicated the strongest correlation coefficient with the highest number of sub-regions in EEA. They found that the pair of sub-regions (W9 and E3 in their Figure 1) best demonstrated the 1-2 day relationship in precipitation between WEA and EEA. The pairs of sub-regions used in the current study (green box and brown box in Figure 1) are in similar locations as W9 and E3 in Figure 1 in Ayesiga et al. (2021). So, sub-region in WEA (green box) for each dataset is used as a sub-region of reference in the spatio-temporal correlation coefficient analysis and the subsequent composite analysis.

One way of assessing the characteristics of a propagating feature is to undertake spatio-temporal correlation coefficient analysis. Figure 1 shows the spatio-temporal correlation coefficient between area averaged time series over the sub-region in WEA (green dashed box) and every grid point in the domain. Day 0 for each data set is shown in the top row and the rest of the lagged sequence at which correlation coefficients are computed increase downwards for each column. In computing the correlation coefficients, the area average time series over the sub-region in WEA (green dashed box) is correlated with the time series of the daily precipitation anomalies at each grid-point, $P_{i,\,j}$ (i=latitude, j=longitude) and then, the time series of each grid-point is shifted so that the sub-region's time series lags the grid point time series by a day at a time. These correlation coefficients are calculated regardless of season and is not conditioned to any propagating tropical disturbance. One sees in Figure 1a-d a coherent eastward propagating signal that has a speed of approximately 7-8° per day. For day 1 (Figure 1b), the positive correlation signal has shifted east and is centered

approximately halfway between where it was located on day 0 and EEA. By day 2 (Figure 1c), the positive correlation signal is seen over EEA while a negative correlation signal dominates WEA and by day 3 (Figure 1d), the positive correlation signal becomes weak and no clear coherent eastward progression is seen. This correlation coefficient pattern (Figure 1a-d) based on 9 years of daily precipitation anomalies including all days from all seasons is similar to that shown in Ayesiga et al. (2021) (their Figure 4, based on 16 years of TRMM)

Looking at Figures 1e-h and i-l, an eastward propagating signal depicted in TRMM (Figure 1a-d) is generally present in the simulated precipitation anomalies. However, from day 0 to day 2 (i.e., Figure 1e-g) while an eastward shift of positive correlation coefficients can be seen, a reversal of the signal over WEA is not seen. Further dissimilarities can also be seen in subsequent days. The propagation speed of the eastward propagating signal in the simulations is not remarkably different from that in the observations. Overall, the results in Figure 1 indicate that, generally, the eastward propagating signal is detectable in the simulated precipitation anomalies as seen in the observations. We tested the sensitivity of the correlation coefficient pattern to the dimensions of the sub-region by repeating the same analysis but using an identical sub-region from TRMM onto the simulated precipitation anomalies and the results were similar (not shown). The generally weak correlation coefficients seen in Figures 1 are not surprising because small spatial and temporal scales affect the strength of individual correlation coefficient. Because these correlation coefficients are statistically significant and spatially coherent signals provides confidence to our results.

To further investigate the eastward propagating signal in the simulated precipitation, Hovmöller plots of CP4A's total precipitation (not shown) showed eastward propagating wet episodes that are similar to those in TRMM (e.g., see Ayesiga et al..,2021; their Figure 6a), a result that is consistent with the eastward propagation correlation coefficient signal shown in Figure 1i-l. Additionally, these plots also showed a strong diurnal cycle and multiple westward propagating

episodes (presumably organised mesoscale convective systems) within envelopes of the eastward propagating wet signal. Our time-longitude plots for precipitation over selected periods (not shown) were similar to that shown in Stratton et al.. (2018; their Fig.9a). The eastward propagating signal shown in Figure 1 may be compared to the eastward propagating convective signal shown in Dunkerton and Crum (1995) and the eastward propagating wet signal shown in Stratton et al. (2018).

b. Kelvin wave activity

An overall picture of the Kelvin wave activity over equatorial Africa is shown in a climatological time-longitude plot of the standard deviation of Kelvin wave divergence in Figure 2. In this figure and other cross-sections, the field(s) are averaged in the latitudinal band 7^{o}about the equator. This averaging range is informed by two aspects. First, Kiladis et al. (2009) showed that strongest signal of Kelvin waves is confined within a latitudinal belt of $\sim 10^{o}$ about the equator (see their Figure 5a). Second, in their recent publication, Ayesiga et al. (2021) analysed the west-east precipitation linkage using sub-regions confined within $\sim 7^{o}$ about the equator. In both ERA-I and model simulations, the first peak of Kelvin wave activity is seen between January-May and the second between September-December. Weak Kelvin wave activity can be seen in relatively dry months (June-August) in both ERA-I and model simulations. In Figure 2, the simulated results are in agreement with those in ERA-I in the sense that there is a signal of Kelvin waves activity over equatorial Africa all year round. Both simulations reasonably capture the overall magnitude of the Kelvin wave activity in ERA-I (Figure 2a). In terms of the spatial distribution, there are visible differences between ERA-I (Figure 2a) and the modelled Kelvin wave activity (Figure 2b and c). For example, Kelvin wave activity in ERA-I shows two longitudinal peaks, a weak peak between 10^{o}E - 20^{o}E and a strong peak between 30^{o}E - 40^{o}E. Both simulations capture the peak Kelvin

wave activity between 30°E - 40°E but their peak activity between 10°E - 20°E is weaker than that in ERA-I. Unlike ERA-I and G25, CP4A (Figure 2c) shows a strong Kelvin wave activity east of about 50°E. This might be due to the presence of the lateral boundary in this model. More generally, the reasons for an underactive Kelvin wave between 10°E - 20°E in both simulations and an overactive Kelvin wave over the Indian Ocean in CP4A remain unclear and beyond the scope of the current study. On comparing the Kelvin wave activity in stitched CP4A (Figure 2c) with that in the complete tropical belt in ERA-I (Figure 2a) and G25 (Figure 2b), it is likely that the stitching had a negligible impact on the coherent propagation of Kelvin wave signal. This is plausible because Kelvin waves are large-scale features and may not be significantly influenced by stitching of the data sets as described in section 2 above.

c. Eastward propagation of observed and modelled precipitation

Figure 3 shows a composite of precipitation anomalies on high amplitude Kelvin wave events of several fields. In both observations (Figure 3a-e) and simulations (Figure 3f-j,k-o), the eastward propagation of positive precipitation anomalies in association with anomalous low-level moisture flux convergence can be seen. Just like in observations, the simulated positive precipitation anomalies and anomalous low-level convergence propagate eastward in association with modelled Kelvin wave convergence (e.g., Figure 3f-j,k-o). As seen in previous observational studies, positive precipitation anomalies are in phase with anomalous low-level westerlies (e.g., Yang et al.. 2007a; Yang et al.. 2009). Figure 3 provides evidence that the eastward propagation of precipitation is well represented in both simulations, and the connection between the simulated precipitation anomalies and Kelvin wave convergence is well captured. While the wind field in G25 is comparable to that in ERA-I, its precipitation signal is generally weak across the entire 5-day sequence, highlighting the likelihood of a weak interaction between the convection and large-scale circulation associated

with Kelvin waves in G25 as seen in other studies of coarse global models (e.g., Yang et al. 2009). Although they did not focus on the role of Kelvin waves in modulating precipitation, Finney et al. (2020) also found that days with anomalous westerly flow experienced enhanced precipitation over EEA. In Figure 3a-e, the Kelvin wave divergence is well aligned with the negative precipitation anomalies however, the negative precipitation anomalies are generally missing in both simulations especially G25. It remains unclear why the suppressed convection is poorly simulated.

d. The horizontal moisture flux and propagation of CCKWs over Equatorial Africa

To gain insight into the sources of moisture associated with the anomalous precipitation signal in Figure 3, Figure 4 shows a lagged composite of anomalous horizontal moisture flux and evolution of CCKW activity at 850 hPa. Figure 4a and 4b, 4f and 4g, 4k and 4l show the horizontal wind structure that is broadly in agreement with the theoretically predicted structure for a Kelvin wave shown in Gill (1980).

ERA-I (Figure 4a-e) displays a coherent eastward propagating moisture flux with the propagation speed consistent with that shown in Figure 1. Recall that Figure 1 is based on precipitation without any conditioning to Kelvin wave events. In essence, Figure 1 and 4 are based on independent analysis methods but exhibit agreement. Also shown in Figure 4 is that the leading edge of the moisture flux is collocated with the Kelvin wave convergence. A day before day 0 (Figure 4a) anomalous moisture flux is seen over the Atlantic ocean and this is followed by low-level westerly anomalies appearing to strengthen between day -1 and day 1. This anomalous westerly flow is seen to advance eastward together with the Kelvin wave convergence and the positive anomalous zonal moisture flux. By days 2 and 3 (Figure 4d and e), an anomalous magnitude of moisture flux, the low-level anomalous westerly flow and the Kelvin wave convergence can be seen over EEA but all

these fields have waned. This result (e.g., Figure 4a-e) suggests that CCKWs modulate low-level moisture flux through anomalous low-level westerly flow.

Comparing the two simulations to ERA-I, one sees that the horizontal structure of the evolution of the Kelvin waves in G25 (Figure 4f-j) is in some aspects similar to that of ERA-I (Figure 4a-e). For example, from day -1 through to day 3, the Kelvin wave convergence is located on the leading edge of the low-level westerly anomalies (vectors) as seen in ERA-I. Also, for G25, the anomalous low-level westerly flow and Kelvin wave convergence appear to weaken on day 2 and 3, a similar evolution can be seen in ERA-I. One key difference between ERA-I and G25 can be seen in Figure 4a and f, in which the the magnitude of the moisture flux in G25 (Figure 4f) is considerably weaker than that in ERA-I (Figure 4a). The other difference that is easily noticeable is that G25 shows a relatively stronger low-level anomalous easterly moisture flux particularly from day -1 to day 1 that extends into the Indian Ocean. The easterly moisture flux anomalies seen in Figure 4f-j may be linked to the persistent positive correlation coefficients in modelled precipitation anomalies seen over EEA in Figure 1e-h. Although CP4A (Figure 4k-o) shows the eastward propagating zonal moisture anomalies that are collocated with eastward moving low-level Kelvin wave convergence, the magnitudes of all the fields are weaker and not as smooth as those in ERA-I and G25. However, CP4A shows anomalous easterly moisture flux that is quantitatively in better agreement to ERA-I than the G25. Figure 4 suggests that both simulations reasonably simulate the Kelvin wave low-level convergence and its eastward propagation phase speed. Easily noticeable is that CP4A shows weaker moisture flux in Figure 4 but stronger pecipitation anomalies in Figure 3. One possible reason for this mismatch might be that the few storms formed in association with the weak moisture flux in CP4A are too intense compared to those in TRMM (Crook et al. 2019).

Table 1 provides an insight on whether the precipitation events (as defined above) are linked to the corresponding Kelvin wave events. Results show that over a period of 9 years, about 53%, 46%

and 62% of the precipitation events during MAM match Kelvin wave events with amplitude above the 60th percentile of the Kelvin wave low-level convergence in ERA, G25 and CP4A respectively. Statistically, for the 60th percentile threshold, the aforementioned percentages would be expected to be only 40% if the match between precipitation events and Kelvin wave events were purely due to random chance (ignoring any possible effects of event clustering). This result suggests that the association between the precipitation events and the Kelvin waves is larger than random chance. In a similar vein, Table 1 suggests a significant number of precipitation events are not related to Kelvin wave events. These are not the focus of the rest of this study but would be a topic to explore in future work.

In comparison with TRMM and CP4A, except for the 95th percentile, G25 (third column in Table 1) shows the lowest number of precipitation events that are also Kelvin wave events. This may be due to the weak interaction between the Kelvin wave dynamics and the precipitation in G25 (implied by the inconsistency between the wind field and the precipitation anomalies in Figure 3). It is possible that the explicit representation of convection in CP4A might have helped in the coupling between the Kelvin waves and the precipitation. To assess the robustness of the results, we looked at the number of precipitation events in TRMM that are also Kelvin wave events in the same season but over a 16 year period (see second column in Table 1). As shown in Table 1, the results over the 16 year period are generally consistent with those over the 9 year period.

e. Composite of the vertical structure of high-amplitude CCKW events

1) Zonal wind and specific humidity

It is important to investigate the vertical structures of the zonal wind and the specific humidity that are associated with the propagation of CCKWs across Equatorial Africa. This is because vertical structures in the zonal wind play a role in the longevity of mesoscale convective systems (e.g.,

Schlueter et al. 2019) while moisture convergence is an important component in the convection-equatorial wave coupling (e.g., Wolding et al. 2020). The vertical section of the composite of anomalous zonal wind and specific humidity on high amplitude Kelvin wave events is shown in Figure 5. Figure 5 shows that in both ERA-I and the simulations, a day before day 0, a westward tilt with height in the anomalous zonal wind and specific humidity develops over the Atlantic Ocean. As the tilted structure propagates into Equatorial Africa, the anomalous westerly flow strengthens on day -1 through to day 1 before becoming weak near the surface on day 2 and 3 as seen in both reanalysis and simulations. The weak westerly anomalies may be linked to the weak positive precipitation anomalies on day 2 (Figure 3d,i,n) and 3 (Figure 3e,j,o).

Figure 5 also shows a leading edge of the anomalous westerly wind that is aligned with the anomalous specific humidity. This is consistent with results in Figure 4 and confirms the connection between the anomalous westerly flow and the transport of moisture from the Atlantic Ocean into the interior of equatorial Africa. On further scrutinising Figure 5, one sees that both ERA-I and the simulations show a drier lower-middle troposphere on day 2 and 3 in comparison to day -1, 0 and 1. We will return to this point in the next subsection. Another noticeable feature shown in both ERA-I and the simulations is that the zonal wind shows an eastward tilt with height above 200hPa, a result that is consistent with Wheeler et al. (2000). This signal may be interpreted to imply the transfer of momentum by anomalous easterly flow into the lower stratosphere (e.g., Yang et al.. 2007a)

The vertical zonal wind and the specific humidity structures shown by the simulations show some differences from those in ERA-I. For example, while the depth of anomalous westerly flow in ERA-I starts from the surface to about 300hPa and the specific humidity anomaly appears to systematically and gradually weaken from day -1 into day 3, G25 shows a shallower and weaker anomalous westerlies particularly on day -1 and day 0 with an extensively moist midtroposphere on

day 1 and 2. In comparison to ERA-I and G25, CP4A also shows shallower and weaker westerly anomalies particularly on day 1 and 2. Although CP4A's anomalous specific humidity is aligned with the leading edge of the weakly tilted zonal wind, its westward tilt with height is incoherent. This notwithstanding, the westward tilt with height and the eastward propagation in the zonal wind field are reasonably captured in both simulations but the magnitude of the anomalous zonal wind is generally weak. The weaker zonal wind anomaly in the simulations may be responsible for weaker moisture flux anomaly shown in Figure 4 for the simulations more especially in CP4A. The vertical structure of specific humidity field is generally poorly simulated in both models particularly CP4A. Because G25 is based on a convection scheme, it is possible that the convection is not sufficiently responding to the large-scale circulation, which then results in errors in the large-scale vertical motion. In CP4A, the source of a poorly simulated vertical structure might be failure of the model to resolve small scale vertical motion or incorrect organisation of individual storms. Also, there are several potential reasons for the discrepancies between models and ERA-I. For example, the weak precipitation signal in G25 (e.g., Figure 3) might cause poor representation of the vertical structure of the zonal wind because the model lacks correct convectively-driven circulations. But also, the weak coupling between the parameterised convection and the moisture field may explain the difference between the vertical profile of the specific humidity in G25 and that in ERA-I. For CP4A, we speculate that the vertical structure of the specific humidity is a response to weaker zonal wind anomalies and/or difficulties in representing shallow convection in the model.

2) Anomalous potential temperature, horizontal mass divergence and zonal-vertical wind

Examining the vertical structure of the potential temperature and the zonal-vertical wind may be useful in understanding convection-wave interactions. The vertical structure composite on high

amplitude Kelvin wave events for anomalous potential temperature, horizontal mass divergence and zonal-vertical wind is shown in Figure 6. ERA-I (Figure 6a-d) displays mid to upper level strong upward motion to the west of relatively weak low-level upward motion. The wind profile in which the low-level inflow is leading upper-level outflow by about 20^{o} (e.g., Figure 6a-c) suggests a westward tilt with height in the zonal-vertical wind structure. A similar tilted zonal-vertical wind structure was found by Wheeler et al. (2000) using NCEP-NCAR reanalysis and Straub and Kiladis (2003) showed similar results using ECMWF's reanalysis. In Figure 6a, b, weak descending motion can be seen east of 30^{o}E. This subsidence is consistent with the negative precipitation anomalies over EEA in Figure 3a, b. The anomalous low-level horizontal mass convergence seen in Figure 6 might be associated with anomalous westerly flow (also see enhanced zonal winds in Figure 5). The tilted anomalous horizontal convergence in Figure 6 matches well with the tilted specific humidity anomalies in Figure 5, suggesting a possible gradual moistening of the troposphere.

As was seen in Figure 5, in Figure 6a-d, a strong and deep anomalous westerly flow is persistently apparent to the west of the location of positive TRMM precipitation anomalies (indicated by a bold purple "X") from day -1 to day 2. It can also be seen from day -1 to day 3 that the regions of upper-level divergence are generally to the west of the region of positive precipitation anomalies (Figure 6a-e), showing the link between precipitation and the convectively coupled circulation.

In Figures 6a-d, vigorous upward motion peaks between 400hPa and 300hPa and roughly coincides with regions of positive precipitation anomalies. By day 3 (Figure 6d) the anomalous westerly flow is weak, and the upward motion is also generally weak or nonexistent. This is consistent with the relatively drier EEA on day 3 in Figure 4e. In Figure 6a-c, the positive potential temperature anomalies between 400hPa-200hPa are nearly collocated with peak upward motion and generally in phase with positive precipitation anomalies. In Figure 6a-d, the surface negative potential temperature anomalies seen to the west of the regions of maximum ascent and positive precipitation

anomalies are suggestive of a cold pool that might be associated with rain-evaporation-forced downdrafts. Although TRMM and ERA-I are obtained from different sources, their alignment shown in Figures 3 and 6a-e suggests our results are robust.

Results in G25 (Figure 6f-j) has some resemblance in some aspects with ERA-I/TRMM in features such as westward tilt with height in the wind field, potential temperature structure and mass divergence. As shown in ERA-I, the tilted horizontal mass convergence in Figure 6 f-i lines up with the tilted anomalous specific humidity in Figure 5f-i. The positive precipitation anomalies are generally collocated with regions of low-level horizontal convergence suggesting that Kelvin wave convergence is likely to be supportive in triggering precipitation as the wave propagates eastward. However, the westerly anomalies in G25 is generally weaker than that in ERA-I. In CP4A (Figure 6k-o), the westward tilt with height in horizontal mass convergence is similar to ERA-I and G25, particularly from day -1 to day 1. The regions of positive precipitation anomalies and negative potential temperature anomalies move together eastward as seen in ERA-I and G25. Also, it can be seen that the low-level negative potential temperature anomalies are generally more realistic in CP4A, although the reason for this remains unclear and may be a subject for future research.

There are some differences between the anomalous zonal-vertical wind structure in CP4A and that in ERA-I. For example, in Figure 6k-m, the circulation west of 10^{o}E appear to be weak and not as consistent as that in the corresponding panels in Figure 6a-c. And in comparison with G25 (Figure 6f-h), CP4A (Figure 6k-m) shows stronger upward motions than that in the corresponding panels of G25. In Figure 6m, vigorous upward motion can be seen between $\sim$ 10^{o}W and 0^{o}and also in proximity of 30^{o}E. Also, in Figure 6n, descending motion between 10^{o}E-20^{o}E is sandwiched by upward motion. The longitudinal distance between the two consecutive regions of upward motion sandwiching the downward motion is much shorter than what is expected of two consecutive phases

of enhanced Kelvin wave-induced convection. This may suggest either the presence of waves of relatively shorter horizontal wavelength than the CCKW or perhaps just more small intense storm clusters as highlighted in Stratton et al. (2018).

3) Interaction of CCKWs with the East African highlands

Guo et al. (2014) suggested that weak amplitude Kelvin waves tend to be associated with a weak westward tilt with height. Here, we have shown in Figures 3 and 4 that Kelvin wave convergence tends to wane over EEA. In this subsection, we explore the clues about the interaction of CCKWs with the East African highlands. In the transition from day 1 (Figure 5c) into day 2 (Figure 5d), the coherent eastward propagating tilted structure of anomalous westerlies appears to get distorted at about 30^{o}E. Furthermore, one can also see in Figure 6c and 6d that the anomalous westerly flow appears not to coherently progress east of about 31^{o}E and the tilt in the vertical structure of the horizontal mass convergence seems weakened and distorted (Figure 6d and 6e) at about the same longitude. Finally, Figure 5 may provide an additional clue about the interaction between topography and the eastward propagation of the CCKW. Considering a generally clear vertical structure of the anomalous specific humidity in Figure 5a-c, Figure 5d shows a fragmented vertical structure of the anomalous specific humidity at 30^{o}E. It can also be seen that the anomalous westerly flow, specific humidity anomalies and Kelvin wave convergence all weaken considerably from day 1 to day 2 (e.g., Figure 6). This is might be because moisture flow is interrupted by the highlands. The distortion of the specific humidity anomalies, mass convergence anomalies and the wind field seen in ERA-I are well captured in both simulations.

The interaction between the anomalous low-level westerlies and the highlands may suggest that the anomalous eastward moisture transport is reduced downstream. Following a suggestion advanced in Guo et al. (2014), we suggest that the obstruction of the tilted zonal-vertical wind

structure may lead to the weakening of the Kelvin wave over EEA. Because the moisture is cut off and the Kelvin wave is weakened, the coupling between the convection and the Kelvin wave is weakened. This may partly explain the drier lower-to middle troposphere seen in Figure 5d,i,n,e,j,o and the weak precipitation anomalies in, for example, Figure 3d and e. The interaction between Kelvin waves and East Africa's highlands is also shown in Matthews (2000). Baranowski et al. (2016) also found a pronounced disintegration of Kelvin waves at about 30^{o}E (e.g., their Figure 6a) and Yang et al. (2021) revealed the influence of East African highlands on the propagation of Kelvin waves in all seasons in both ERA-I and their model simulations.

4. Discussion and Conclusions

In this study, the physical processes through which Convectively Coupled Kelvin Waves modulate the eastward propagation of precipitation across Equatorial Africa are investigated using a multi-year state-of-the-art Convection permitting simulation (CP4A), a relatively coarse resolution global simulation (G25), observations (TRMM) and reanalysis (ERA-I). The fidelity of CP4A and G25 in representing the dynamical structure of Kelvin wave events in the context of WEA-EEA convection and precipitation connection is evaluated.

It is found that the two important related processes through which CCKWs influence the propagation of convection and precipitation from west to east across Equatorial Africa are:1) low-level westerly anomalies that lead to increased low-level convergence and, 2) westerly moisture flux anomalies that amplify the lower-to-mid-tropospheric specific humidity. These findings suggest that the important processes through which CCKWs modulate the eastward propagation of precipitation across Equatorial Africa are low-level moisture flux convergence and modification of lower-to-midtropospheric moisture.

Results from evaluation of CP4A and G25 in representing the dynamical structure of Kelvin wave events in the context of WEA-EEA convection and precipitation connection against TRMM and ERA-I show that both models capture the key features of propagation of CCKWs across equatorial Africa. However, G25 simulates a precipitation field that is weaker than that in TRMM while CP4A shows westerly anomalies that are too weak and shallow but the precipitation field is better simulated. In general, both models capture the eastward propagation of precipitation anomalies in association with Kelvin wave convergence. We believe that this is the first study over Equatorial Africa to use the precipitation field and Kelvin wave activity based on dynamical fields to: a) explore the connection between the Kelvin waves and the eastward propagating precipitation signal and the associated processes, and b) evaluate a multi-year state-of-the-art simulation from a convection permitting model.

Correlation coefficient analysis of daily precipitation anomalies for both observations (TRMM) and model simulations (CP4A and G25) shows an eastward propagating feature whose speed is about 7-8^{o}per day (e.g., Figure 1), suggesting a large-scale feature acting to organise precipitation. This result may be compared to an eastward propagating convective signal found in OLR in Mekonnen and Thorncroft (2016).

To explore the eastward propagation of precipitation across Equatorial Africa by gaining an insight into the number of days when precipitation is presumed to propagate eastward, we have used a percentile threshold to count the number of precipitation events based on a pair of sub-regions. We show in Table 1 the percentage of precipitation events that might be related to Kelvin wave events (see section 3 for the definition of the precipitation events and a Kelvin wave event). Results in Table 1 imply that, for example, over a period of 9 years, about 53%, 46% and 62% of the precipitation events during MAM are related to Kelvin waves low-level convergence above the 60th percentile of the Kelvin wave low-level convergence in ERA, G25 and CP4A respectively. This

means that, generally, the probability of a precipitation event being associated with a Kelvin wave event in both observations and simulations exceeds one that is expected by chance, and confirms that precipitation events in MAM are often related to Kelvin wave events (e.g., Huang and Huang 2011; Laing et al. 2011). In Baranowski et al. (2020), Kelvin waves past Sumatra were found to be solely responsible for about 30% of anomalous precipitation events, suggesting that not all precipitation events are linked to Kelvin wave events.

The climatological variability of Kelvin wave activity across Equatorial Africa is shown in Figure 2. The Kelvin wave activity as depicted in ERA-I and both simulations, with a peak in MAM, is generally consistent with results in Roundy and Frank (2004) and Huang and Huang (2011, their Fig.5d) (e.g., Figure 2a). Notwithstanding the underactive Kelvin waves between $\sim 10^{o}$E-20^{o}E, both simulations generally capture the spatial and temporal variability of Kelvin wave activity as shown in ERA-I. This result is in agreement with results in Jackson et al. (2019) who found that the G25 simulated CCKWs with amplitude close to observations. The two peaks of Kelvin wave activity shown in Figure 2 coincide with Africa's two equatorial rainfall seasons that follow the north-south migration of the ITCZ, highlighting a likely connection between Kelvin wave activity and the ITCZ (e.g., Dias and Pauluis 2011).

While our results show evidence of anomalous westerly moisture flux, this might be enhancing the locally available moisture (e.g., Pokam et al. 2012). By compositing the wind and specific humidity field on high amplitude Kelvin waves, we show that 1 day before day 0, the anomalous zonal flow over the Atlantic Ocean is strengthened (e.g., Figure. 4a,b and Figure 5a,b). This leads to low-level convergence as shown in the entire sequence (e.g., Figure 4a-e, f-j and k-o). At the eastern edge of the westerly anomalies there is enhanced anomalous convergence. This low-level convergence is important because it provides an environment favourable for convection. Figures 4, 5, and 6 reveal that the anomalous low-level westerly flow transports moisture into a region of

Kelvin wave low-level convergence and positive precipitation anomalies (e.g., Straub and Kiladis 2003), suggesting that the Kelvin wave-precipitation coupling is supported by an enhanced supply of moisture (e.g., Wolding et al. 2020).

From the co-location of the modelled Kelvin wave low-level convergence and the simulated precipitation anomalies (e.g., Figure 3) we show that the simulations examined in this study reasonably represent an eastward propagating convective and precipitation signal that is associated with CCKWs previously only found in observational studies. We will return to this result later. In comparison to G25, CP4A indicated a better representation of precipitation (e.g.,Figure 3) which demonstrates the value of explicit representation of convection. The better representation of daily precipitation in CP4A in comparison to simulations in which convection was parameterised has been shown in previous other studies such as Stratton et al. (2018), Finney et al. (2019) and Berthou et al. (2019).

The eastward propagation of convection and precipitation require successive formation of new convective cells to the east of deep convective systems (e.g., Nakazawa 1988). The anomalous zonal-vertical wind structure in ERA-I (Figure 6) reveals weak upward motion that develops into strong mid-to upper tropospheric upward motion. This is indicative of shallow convection at the leading edge of deep convection. Despite the weak zonal-vertical circulation in G25, both simulations generally reproduce the zonal-vertical wind structure that is qualitatively similar to that in ERA-I.

We also show that Kelvin wave convergence tends to weaken over EEA (e.g., Figures 3 and 4) (e.g., Mounier et al. 2007; Nguyen and Duvel 2008). Also, anomalous low-level westerly flow appears not to coherently progress east of about 30^{o}E (e.g., Figures 5 and 6). The highlands on the western branch of the East African rift valley appear to distort the coherent eastward propagation of the tilted structure of both the anomalous westerly flow and specific humidity thereby impacting

the supply of moisture as the CCKW approaches EEA (e.g., Dunkerton and Crum 1995; Matthews 2000). Once large-scale low-level horizontal convergence is distorted and at the same time the supply of moisture is possibly diminished, the precipitation signal over EEA weakens. We suggest that a weak CCKW over EEA may be partly associated with a weakened westward tilt with height in dynamical fields and anomalous specific humidity (e.g., Guo et al. 2014).

The co-location of modelled positive precipitation anomalies and the corresponding Kelvin wave low-level convergence (e.g., Figure 3f-j, 3k-o) is consistent with results in observational studies that found an association between convective activity and Kelvin waves over Equatorial Africa (e.g., Nguyen and Duvel 2008; Laing et al. 2011; Mekonnen and Thorncroft 2016). However, the anomalous precipitation signal in G25 is much weaker than the observed. The weak precipitation signal in G25 is not surprising because previous studies such as Stephens et al. (2010) reported that rainfall in GCMs tends to be frequent and weak. As earlier discussed, although the Kevin wave activity in G25 matches that in ERA-I, the composite of precipitation anomalies on high-amplitude Kelvin wave events displays a precipitation signal in G25 (e.g., Figure 3f-j) that is weaker than that in TRMM (e.g., Figure 3a-e). This likely indicates too-weak coupling between the precipitation and Kelvin waves in G25 (e.g., Yang et al. 2009; Straub et al. 2010). This is supported by the results in Table 1 (fourth column) that show a smaller percentage of precipitation events that are also Kelvin wave events in G25. The anomalous precipitation signal in CP4A nearly matches that in ERA-I especially on day 2 (e.g., Figure 3c and m). Generally, both CP4A and G25 capture the eastward propagation of precipitation as shown in TRMM (e.g., Figure 1 and 3) and the role of CCKWs in modulating the West-East propagation of precipitation is well simulated.

In agreement with Zebaze et al. (2017), our results in both observations and simulations show that CCKWs influence zonal flow and in turn modulate the advection of moisture into regions of convective activity and precipitation (e.g., Figures 3-6). Much of the anomalous moisture

that is supporting the eastward propagation of precipitation appears to be transported from the Atlantic Ocean as compared to the Indian Ocean (e.g., Figure 4). Berhane et al. (2015) and Finney et al. (2020) have also documented enhanced rainy days over EEA that are associated with low-level westerly wind anomalies. The implication is that low-level circulation plays a key role in precipitation variability over Equatorial Africa.

Both CP4A and G25 portray a westward tilt with height in the anomalous zonal wind and specific humidity (e.g., Figures 5 and 6), which provides evidence of the presence of a Kelvin wave signal in the model simulations that is broadly comparable to that in ERA-I (e.g., Wheeler et al. 2000; Straub and Kiladis 2002; Frierson 2007; Tulich and Mapes 2008). Both models reasonably simulate key features of CCKWs in the sense that they both reveal low-level anomalous westerly flow that is in phase with positive precipitation anomalies (e.g., Figures 3 and 6) (e.g., Yang et al. 2009).

The negative potential temperature anomalies (e.g., Figure 6) shown to the west of the positive precipitation anomalies may be interpreted to be a result of descending cold and dry air resulting from evaporative cooling of stratiform precipitation, suggesting an involvement of diabatic processes as documented in Kiladis et al. (2005). In comparison to G25, the low-level negative potential temperature anomalies appear to be more realistic in CP4A, probably because of more reastically complete convective features (e.g., day 1-3 in Figure 6). Unlike CP4A, G25 fails to simulate the negative potential temperature anomalies (e.g., Figure 6f-j). This might be due to its deficiency in realistically simulating convection in G25 (e.g., Thayer-Calder and Randall 2012). It is important to note that for comparison purposes, we have used ERA-I as a proxy to observations. The caveat here is that a convection scheme was used in the production of ERA-I, thus our results need to be interpreted with this in mind.

Modelling results in this study provide support to observational studies such as Mekonnen and Thorncroft (2016) in that the interaction they found in cloud brightness temperature is also present

in modelled precipitation. The operational forecasting community need to pay attention to the daily Kelvin wave activity. However, our results also reveal that some precipitation events are not related to Kelvin wave events. Future work needs to investigate this aspect. Additionally, we have explored some clues that suggest that the East African highlands interfere with the coherent eastward propagation of CCKWs. Model experiments with a focus on the sensitivity of the eastward propagating Kelvin waves to orographic effects of the East African highlands may be useful in exploring the extent to which these highlands interact with CCKWs.

Acknowledgments

GA was funded by the University of Reading International Research Studentship and Government of Republic of Uganda through Uganda National Meteorological Authority (UNMA). CJRW acknowledges the financial support of the UK Natural Environment Research Council-funded SWEET project (Super-Warm Early Eocene Temperatures), research grant NE/P01903X/1. G-YY was supported by the National Centre for Atmospheric Science ODA national capability programme ACREW (NE/R000034/1), which is supported by NERC and the GCRF. RS was supported by the National Environmental Research Council/Department for International Development via the Future Climate for Africa (FCFA) funded project Improving Model Processes for African Climate (IMPALA: NE/M017265/1). MR was supported by the Met Office Hadley Centre Climate Programme funded by BEIS and Defra (GA01101). The authors are grateful to Improving Model Processes for African Climate (IMPALA) project for providing the CP4A simulation and MR (Met Office) for running and providing access to the G25. The authors are grateful to Prof. Emily Black, Prof. Andrew Turner, Prof. Steve Woolnough and Dr. Linda Hirons for useful discussions. We also thank two anonymous reviewers for insightful comments that helped improve the manuscript.

None of the authors of this study have any conflict of interest to declare.

Data Statement

The authors express sincere appreciation to NASA for TRMM 3B42, version 7 and ECMWF for ERA-I. Both TRMM and ERA-Interim are publicly available. The ERA-I based equatorial wave dataset was produced as part of the Newton Fund project under the auspices of the WCSSP Southeast Asia project by the third co-author and is available on http://gws-access.ceda.ac.uk/public/ncas_climate/seasia_waves/historical_waves. The CP4-Africa dateset generated under the FCFA IMPALA project is publicly available from the Centre for Environmental Data Analysis (CEDA) archive (http://archive.ceda.ac.uk/). The global model simulation (G25) used in this study can be accessed on request from the fifth co-author.

References

Ayesiga, G., C. E. Holloway, C. J. Williams, G.-Y. Yang, and S. Ferrett, 2021: The observed synoptic scale precipitation relationship between Western Equatorial Africa and Eastern Equatorial Africa. *International Journal of Climatology*, **41**, E582–E601.

Baranowski, D. B., M. K. Flatau, P. J. Flatau, and A. J. Matthews, 2016: Impact of atmospheric convectively coupled equatorial Kelvin waves on upper ocean variability. *Journal of Geophysical Research: Atmospheres*, **121 (5)**, 2045–2059.

Baranowski, D. B., and Coauthors, 2020: Social-media and newspaper reports reveal large-scale meteorological drivers of floods on Sumatra. *Nature communications*, **11 (1)**, 1–10.

Berhane, F., B. Zaitchik, and H. S. Badr, 2015: The Madden–Julian Oscillation's influence on spring rainy season precipitation over equatorial West Africa. *Journal of Climate*, **28 (22)**, 8653–8672.

826 Berthou, S., D. P. Rowell, E. J. Kendon, M. J. Roberts, R. A. Stratton, J. A. Crook, and C. Wilcox,
827 2019: Improved climatological precipitation characteristics over West Africa at convection-
828 permitting scales. *Climate Dynamics*, **53 (3)**, 1991–2011.

829 Crook, J., C. Klein, S. Folwell, C. M. Taylor, D. J. Parker, R. Stratton, and T. Stein, 2019:
830 Assessment of the representation of West African storm lifecycles in convection-permitting
831 simulations. *Earth and Space Science*, **6 (5)**, 818–835.

832 Dee, D. P., and Coauthors, 2011: The ERA-Interim reanalysis: Configuration and performance of
833 the data assimilation system. *Quarterly Journal of the royal meteorological society*, **137 (656)**,
834 553–597.

835 Dezfuli, A. K., B. F. Zaitchik, and A. Gnanadesikan, 2015: Regional atmospheric circulation and
836 rainfall variability in south equatorial Africa. *Journal of Climate*, **28 (2)**, 809–818.

837 Dias, J., and O. Pauluis, 2011: Modulations of the phase speed of convectively coupled Kelvin
838 waves by the ITCZ. *Journal of the atmospheric sciences*, **68 (7)**, 1446–1459.

839 Dunkerton, T. J., and F. X. Crum, 1995: Eastward propagating 2-to 15-day equatorial convec-
840 tion and its relation to the tropical intraseasonal oscillation. *Journal of Geophysical Research:*
841 *Atmospheres*, **100 (D12)**, 25 781–25 790.

842 FAO, I., 2016: WFP. The State of Food Insecurity in the World: Meeting the 2015 international
843 hunger targets: taking stock of uneven progress. 2015. I4646E/1/05.15.

844 Ferrett, S., G.-Y. Yang, S. J. Woolnough, J. Methven, K. Hodges, and C. E. Holloway, 2020:
845 Linking extreme precipitation in Southeast Asia to equatorial waves. *Quarterly Journal of the*
846 *Royal Meteorological Society*, **146 (727)**, 665–684.

Finney, D. L., J. H. Marsham, D. P. Walker, C. E. Birch, B. J. Woodhams, L. S. Jackson, and S. Hardy, 2020: The effect of westerlies on East African rainfall and the associated role of tropical cyclones and the Madden–Julian Oscillation. *Quarterly Journal of the Royal Meteorological Society*, **146 (727)**, 647–664.

Finney, D. L., and Coauthors, 2019: Implications of improved representation of convection for the east africa water budget using a convection-permitting model. *Journal of Climate*, **32 (7)**, 2109–2129.

Frierson, D. M., 2007: Convectively coupled Kelvin waves in an idealized moist general circulation model. *Journal of the atmospheric sciences*, **64 (6)**, 2076–2090.

Fritsch, J., and C. Chappell, 1980: Numerical prediction of convectively driven mesoscale pressure systems. Part i: Convective parameterization. *Journal of Atmospheric Sciences*, **37 (8)**, 1722–1733.

Gill, A. E., 1980: Some simple solutions for heat-induced tropical circulation. *Quarterly Journal of the Royal Meteorological Society*, **106 (449)**, 447–462.

Grant, A., 2001: Cloud-base fluxes in the cumulus-capped boundary layer. *Quarterly Journal of the Royal Meteorological Society*, **127 (572)**, 407–421.

Gregory, D., and P. Rowntree, 1990: A mass flux convection scheme with representation of cloud ensemble characteristics and stability-dependent closure. *Monthly Weather Review*, **118 (7)**, 1483–1506.

Guo, Y., X. Jiang, and D. E. Waliser, 2014: Modulation of the convectively coupled kelvin waves over South America and the tropical Atlantic Ocean in association with the Madden–Julian Oscillation. *Journal of the Atmospheric Sciences*, **71 (4)**, 1371–1388.

869 Huang, P., C. Chou, and R. Huang, 2013: The activity of convectively coupled equatorial waves
870 in CMIP3 global climate models. *Theoretical and applied climatology*, **112 (3-4)**, 697–711.

871 Huang, P., and R. Huang, 2011: Climatology and interannual variability of convectively coupled
872 equatorial waves activity. *Journal of climate*, **24 (16)**, 4451–4465.

873 Huffman, G. J., and Coauthors, 2007: The trmm multisatellite precipitation analysis (tmpa):
874 Quasi-global, multiyear, combined-sensor precipitation estimates at fine scales. *Journal of hy-*
875 *drometeorology*, **8 (1)**, 38–55.

876 Jackson, L. S., R. J. Keane, D. L. Finney, J. H. Marsham, D. J. Parker, C. A. Senior, and R. A.
877 Stratton, 2019: Regional differences in the response of rainfall to convectively coupled Kelvin
878 waves over tropical Africa. *Journal of Climate*, **32 (23)**, 8143–8165.

879 Kiladis, G. N., K. H. Straub, and P. T. Haertel, 2005: Zonal and vertical structure of the Madden–
880 Julian Oscillation. *Journal of the atmospheric sciences*, **62 (8)**, 2790–2809.

881 Kiladis, G. N., M. C. Wheeler, P. T. Haertel, K. H. Straub, and P. E. Roundy, 2009: Convectively
882 coupled equatorial waves. *Reviews of Geophysics*, **47 (2)**.

883 Laing, A. G., R. E. Carbone, and V. Levizzani, 2011: Cycles and propagation of deep convection
884 over equatorial Africa. *Monthly weather review*, **139 (9)**, 2832–2853.

885 Matthews, A. J., 2000: Propagation mechanisms for the Madden-Julian Oscillation. *Quarterly*
886 *Journal of the Royal Meteorological Society*, **126 (569)**, 2637–2651.

887 Mekonnen, A., and C. D. Thorncroft, 2016: On mechanisms that determine synoptic time scale
888 convection over East Africa. *International Journal of Climatology*, **36 (12)**, 4045–4057.

Mekonnen, A., C. D. Thorncroft, A. R. Aiyyer, and G. N. Kiladis, 2008: Convectively coupled Kelvin waves over tropical Africa during the boreal summer: Structure and variability. *Journal of Climate*, **21 (24)**, 6649–6667.

Mounier, F., G. N. Kiladis, and S. Janicot, 2007: Analysis of the dominant mode of convectively coupled kelvin waves in the West African monsoon. *Journal of climate*, **20 (8)**, 1487–1503.

Nakazawa, T., 1988: Tropical super clusters within intraseasonal variations over the western Pacific. *Journal of the Meteorological Society of Japan. Ser. II*, **66 (6)**, 823–839.

Nguyen, H., and J.-P. Duvel, 2008: Synoptic wave perturbations and convective systems over equatorial Africa. *Journal of climate*, **21 (23)**, 6372–6388.

Nicholson, S. E., 2017: Climate and climatic variability of rainfall over eastern Africa. *Reviews of Geophysics*, **55 (3)**, 590–635.

Nicholson, S. E., and A. K. Dezfuli, 2013: The relationship of rainfall variability in western equatorial Africa to the tropical oceans and atmospheric circulation. Part I: The boreal spring. *Journal of climate*, **26 (1)**, 45–65.

Pokam, W. M., L. A. T. Djiotang, and F. K. Mkankam, 2012: Atmospheric water vapor transport and recycling in equatorial Central Africa through ncep/ncar reanalysis data. *Climate Dynamics*, **38 (9)**, 1715–1729.

Roundy, P. E., and W. M. Frank, 2004: A climatology of waves in the equatorial region. *Journal of the atmospheric sciences*, **61 (17)**, 2105–2132.

Schlueter, A., 2020: Synoptic to intraseasonal variability of African rainfall. *Oxford Research Encyclopedia of Climate Science*, Oxford University Press.

Schlueter, A., A. H. Fink, and P. Knippertz, 2019: A systematic comparison of tropical waves over northern Africa. Part II: Dynamics and thermodynamics. *Journal of Climate*, **32 (9)**, 2605–2625.

Smith, R., 1990: A scheme for predicting layer clouds and their water content in a general circulation model. *Quarterly Journal of the Royal Meteorological Society*, **116 (492)**, 435–460.

Stephens, G. L., and Coauthors, 2010: Dreary state of precipitation in global models. *Journal of Geophysical Research: Atmospheres*, **115 (D24)**.

Stratton, R. A., and Coauthors, 2018: A Pan-African convection-permitting regional climate simulation with the met office unified model: CP4-Africa. *Journal of Climate*, **31 (9)**, 3485–3508.

Straub, K. H., P. T. Haertel, and G. N. Kiladis, 2010: An analysis of convectively coupled Kelvin waves in 20 WCRP CMIP3 global coupled climate models. *Journal of climate*, **23 (11)**, 3031–3056.

Straub, K. H., and G. N. Kiladis, 2002: Observations of a convectively coupled Kelvin wave in the eastern Pacific ITCZ. *Journal of the atmospheric sciences*, **59 (1)**, 30–53.

Straub, K. H., and G. N. Kiladis, 2003: Extratropical forcing of convectively coupled Kelvin waves during austral winter. *Journal of the atmospheric sciences*, **60 (3)**, 526–543.

Thayer-Calder, K., and D. Randall, 2012: A Convective Downdraft Prameterization Guided By High-Resolution Cloud Modeling. *AGU Fall Meeting Abstracts*, Vol. 2012, A53F–0189.

Tulich, S. N., G. N. Kiladis, and A. Suzuki-Parker, 2011: Convectively coupled Kelvin and easterly waves in a regional climate simulation of the tropics. *Climate dynamics*, **36 (1-2)**, 185–203.

Tulich, S. N., and B. E. Mapes, 2008: Multiscale convective wave disturbances in the tropics: Insights from a two-dimensional cloud-resolving model. *Journal of the atmospheric sciences*, **65 (1)**, 140–155.

Walters, D., and Coauthors, 2019b: The Met Office Unified Model Global Atmosphere 7.0/7.1 and JULES Global Land 7.0 configurations. *Geoscientific Model Development*, **12 (5)**, 1909–1963.

Wang, L., and T. Li, 2017: Convectively coupled Kelvin waves in CMIP5 coupled climate models. *Climate Dynamics*, **48 (3-4)**, 767–781.

Wheeler, M., G. N. Kiladis, and P. J. Webster, 2000: Large-scale dynamical fields associated with convectively coupled equatorial waves. *Journal of the Atmospheric Sciences*, **57 (5)**, 613–640.

Wheeler, M., and H. Nguyen, 2015: Tropical meteorology and climate| equatorial waves. *Encyclopedia of Atmospheric Sciences 2nd Edition, volume 6*.

Wilson, D. R., A. C. Bushell, A. M. Kerr-Munslow, J. D. Price, and C. J. Morcrette, 2008: Pc2: A prognostic cloud fraction and condensation scheme. I: Scheme description. *Quarterly Journal of the Royal Meteorological Society: A journal of the atmospheric sciences, applied meteorology and physical oceanography*, **134 (637)**, 2093–2107.

Wolding, B., J. Dias, G. Kiladis, E. Maloney, and M. Branson, 2020: Interactions between moisture and tropical convection. Part II: The convective coupling of equatorial waves. *Journal of the Atmospheric Sciences*, **77 (5)**, 1801–1819.

Yang, G.-Y., S. Ferrett, S. Woolnough, J. Methven, and C. Holloway, 2021: Real-time identification of equatorial waves and evaluation of waves in global forecasts. *Weather and Forecasting*, **36 (1)**, 171–193.

951 Yang, G.-Y., and B. Hoskins, 2013: ENSO impact on Kelvin waves and associated tropical
952 convection. *Journal of the atmospheric sciences*, **70 (11)**, 3513–3532.

953 Yang, G.-Y., B. Hoskins, and L. Gray, 2012: The influence of the QBO on the propagation of
954 equatorial waves into the stratosphere. *Journal of the atmospheric sciences*, **69 (10)**, 2959–2982.

955 Yang, G.-Y., B. Hoskins, and J. Slingo, 2003: Convectively coupled equatorial waves: A new
956 methodology for identifying wave structures in observational data. *Journal of the atmospheric*
957 *sciences*, **60 (14)**, 1637–1654.

958 Yang, G.-Y., B. Hoskins, and J. Slingo, 2007a: Convectively coupled equatorial waves. Part I:
959 Horizontal and vertical structures. *Journal of the atmospheric sciences*, **64 (10)**, 3406–3423.

960 Yang, G.-Y., and B. J. Hoskins, 2016: ENSO-related variation of equatorial MRG and Rossby
961 waves and forcing from higher latitudes. *Quarterly Journal of the Royal Meteorological Society*,
962 **142 (699)**, 2488–2504.

963 Yang, G.-Y., B. J. Hoskins, and J. M. Slingo, 2011: Equatorial waves in opposite QBO phases.
964 *Journal of the Atmospheric Sciences*, **68 (4)**, 839–862.

965 Yang, G.-Y., J. Methven, S. Woolnough, K. Hodges, and B. Hoskins, 2018: Linking african
966 easterly wave activity with equatorial waves and the influence of Rossby waves from the Southern
967 Hemisphere. *Journal of Atmospheric Sciences*, **75 (6)**, 1783–1809.

968 Yang, G.-Y., J. Slingo, and B. Hoskins, 2009: Convectively coupled equatorial waves in high-
969 resolution Hadley Centre climate models. *Journal of climate*, **22 (8)**, 1897–1919.

970 Zebaze, S., A. Lenouo, C. Tchawoua, A. T. Gaye, and F. M. Kamga, 2017: Interaction between
971 moisture transport and Kelvin waves events over Equatorial Africa through ERA-interim. *Atmo-*
972 *spheric Science Letters*, **18 (7)**, 300–306.

LIST OF TABLES

TABLE 1. Percentage of precipitation events that are also Kelvin wave events in MAM based on exceedance of a particular threshold of low-level Kelvin wave convergence for TRMM, G25 and CP4A. A 16 year period (1998-2013) was used for events in the second column while a 9 year period (1998-2006) was used for the three columns on the right.

Percentiles (Kelvin conv threshold)	**TRMM (16 year period)**	**TRMM**	**G25**	**CP4A**
95	18.8	23.6	12.5	10.8
90	32.9	40.0	16.7	21.6
85	44.7	45.5	16.7	35.1
80	51.8	47.3	29.2	43.2
75	55.3	49.1	33.3	45.9
70	56.5	49.1	37.5	56.8
65	57.6	49.1	45.8	62.2
60	61.2	52.7	45.8	62.2

LIST OF FIGURES

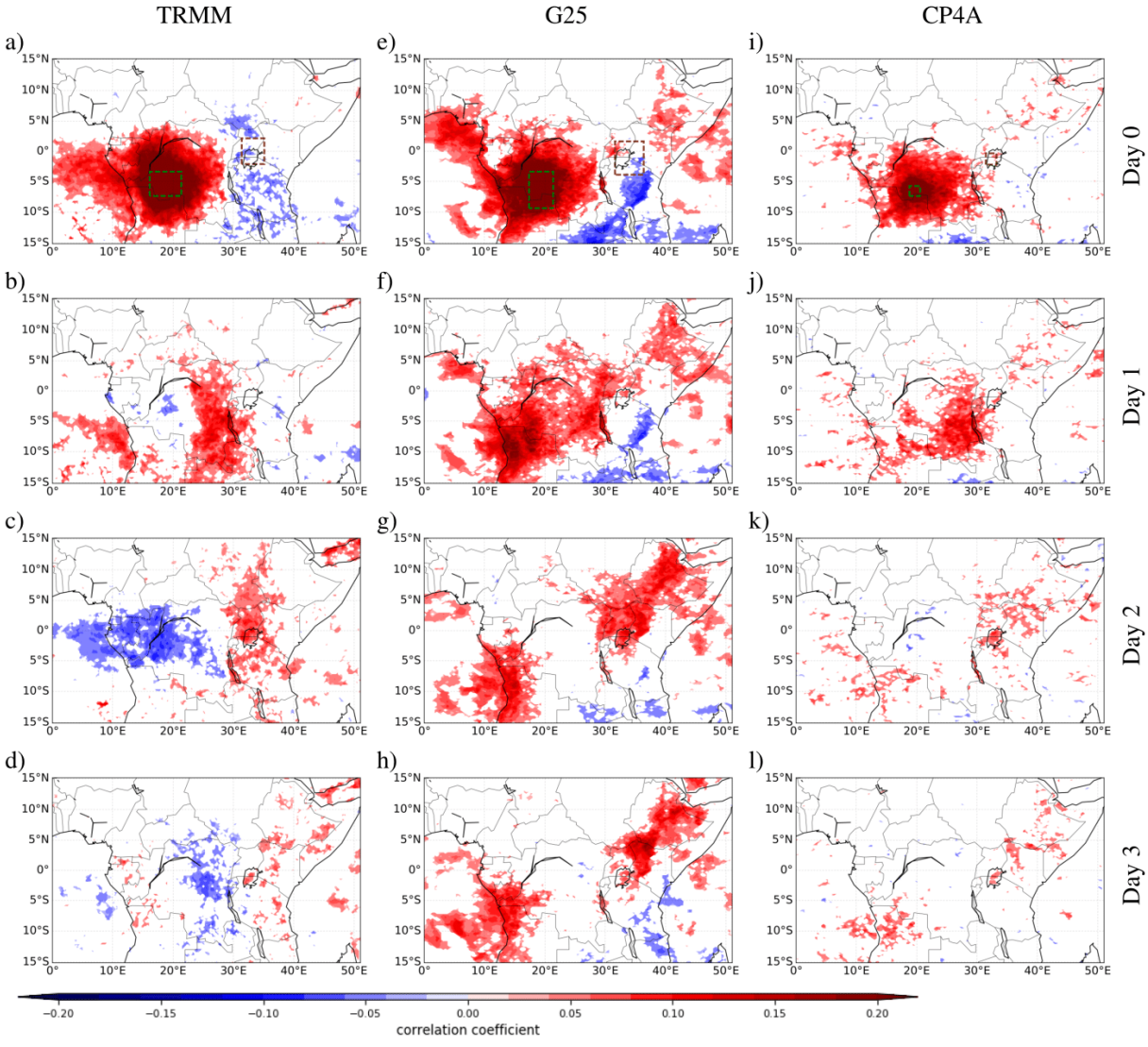

1024 FIG. 1. Lagged correlation coefficients between respective sub-region's (dashed green box in the top panels)
1025 area average time series and every grid point for (a)-(d) TRMM, (e)-(h) G25 and (i)-(l) CP4A based on 9 years
1026 of daily precipitation anomalies. The lags for which the correlation coefficients are calculated are shown on
1027 the right of each row. Correlation coefficients are calculated regardless of season and the shading shows the
1028 correlation coefficients that are statistically significant at 95% confidence level.

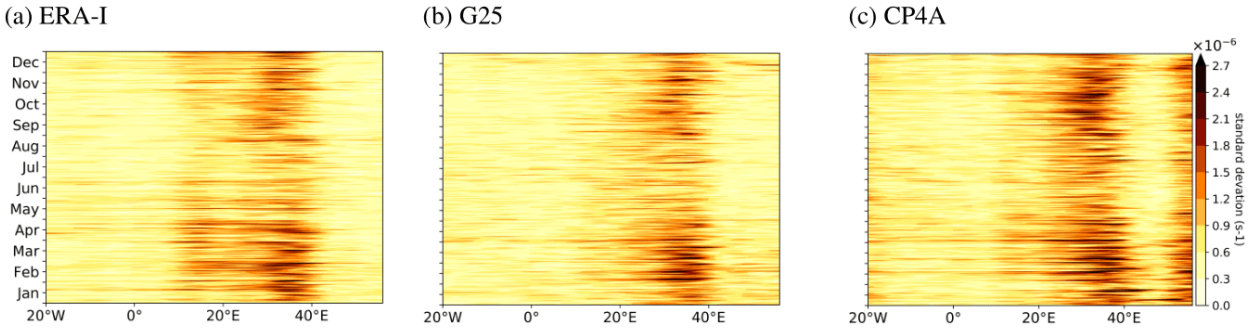

FIG. 2. The seasonal cycle of Kelvin wave activity for (a) ERA-I (b) G25 and (c) CP4A as depicted by standard deviation of Kelvin wave 850 hPa divergence for 1998-2006. Kelvin wave divergence is latitudinally averaged over 7°S-7°N before calculating the standard deviation.

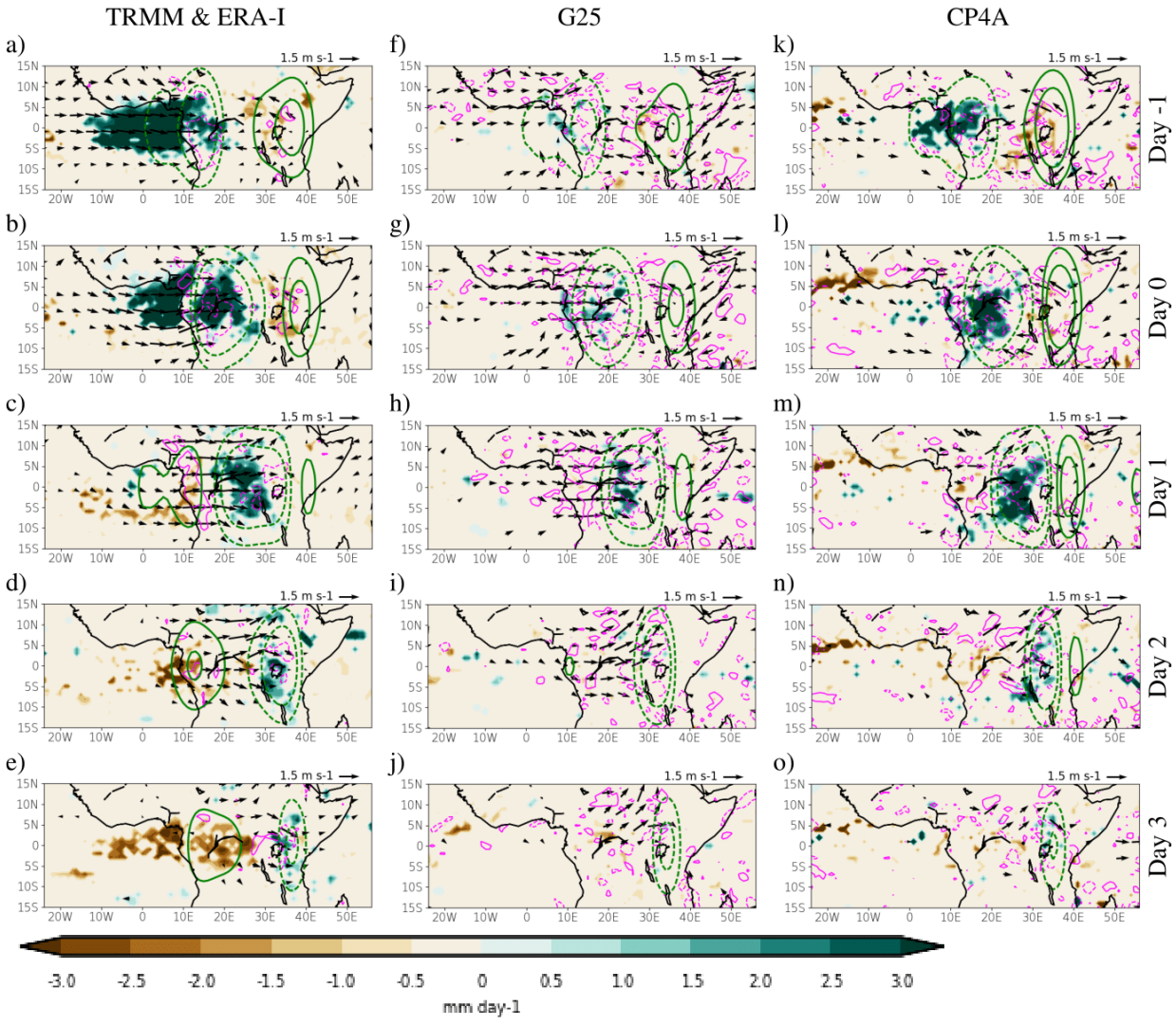

1032 FIG. 3. The lagged high-amplitude Kelvin wave event composite for (a-e) TRMM and ERA-I, (f-j) G25 and
1033 (k-o) CP4A, showing Kelvin wave low-level convergence (green dashed contours) and divergence (green solid
1034 contours), daily precipitation anomalies (shading), and 850 hPa wind anomalies (vectors). The lags for which a
1035 composite was computed are shown on the right of each row. Precipitation anomalies (shading) are plotted if
1036 statistically significant at 95% confidence level. Contour interval for divergence is 4 x 10^{-7} s^{-1} and wind vectors
1037 are plotted if zonal or meridional component is statistically significant at 95% confidence level. 850 hPa moisture
1038 flux divergence is shown with thin magenta contours (solid is divergence, dashed is convergence). Only the -2 x
1039 10^{-8} and 2 x 10^{-8} kg kg^{-1} s^{-1} contours are shown.

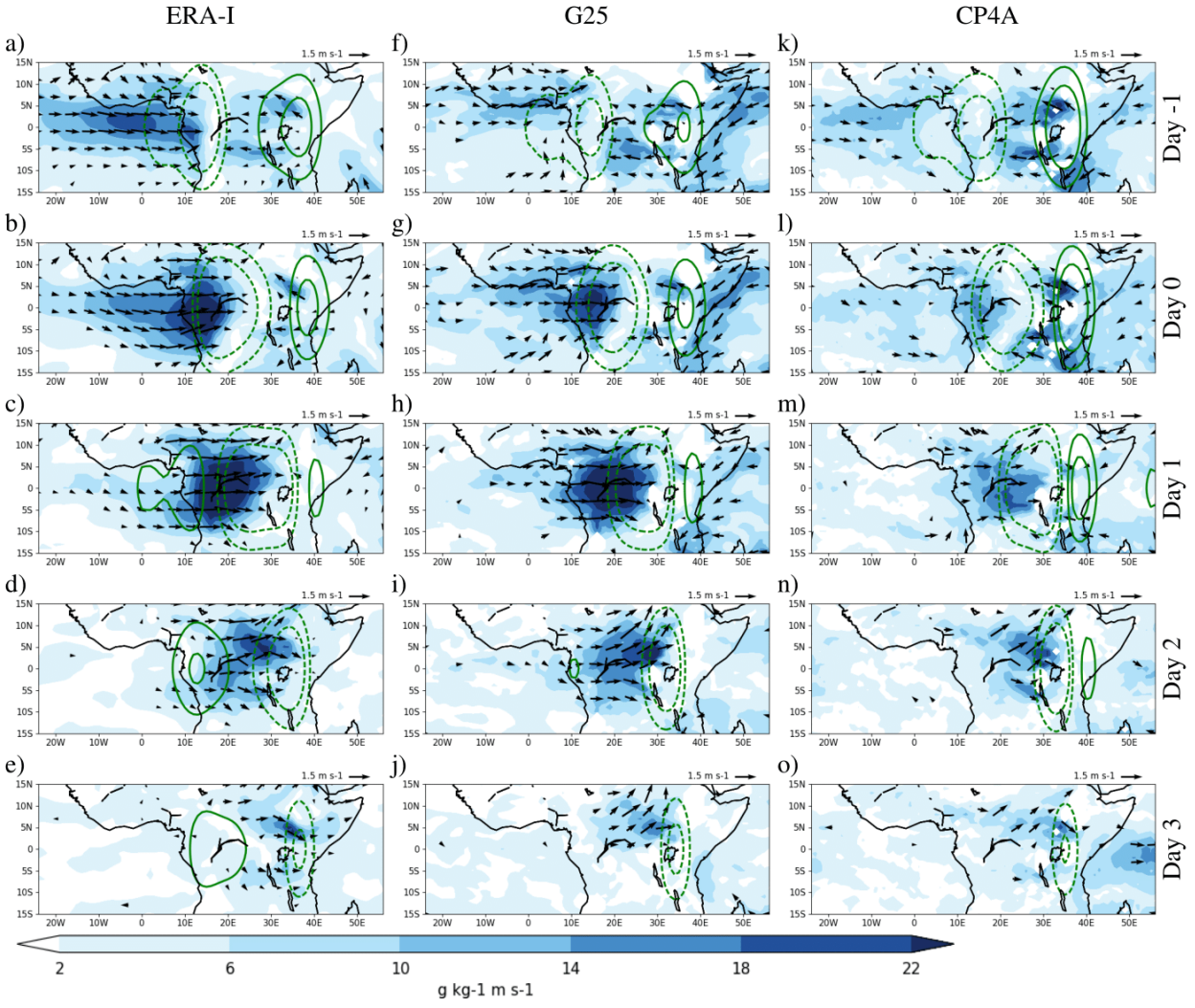

1040 FIG. 4. The 850 hPa lagged high-amplitude Kelvin wave event composite for (a-e) ERA-I, (f-j) G25 and
1041 (k-o) CP4A, Kelvin wave low-level convergence (green dashed contours) and divergence (green solid contours),
1042 magnitude of the anomalous 850 hPa horizontal moisture flux (shaded) and 850 hPa wind anomalies (vectors).
1043 The lags for which a composite was computed are shown on the right of each row. Contour interval for divergence
1044 is 4 x 10^{-7} s^{-1} and wind vectors are plotted if zonal or meridional component is statistically significant at 95%
1045 confidence level. Reference wind is shown at the top right of each panel.

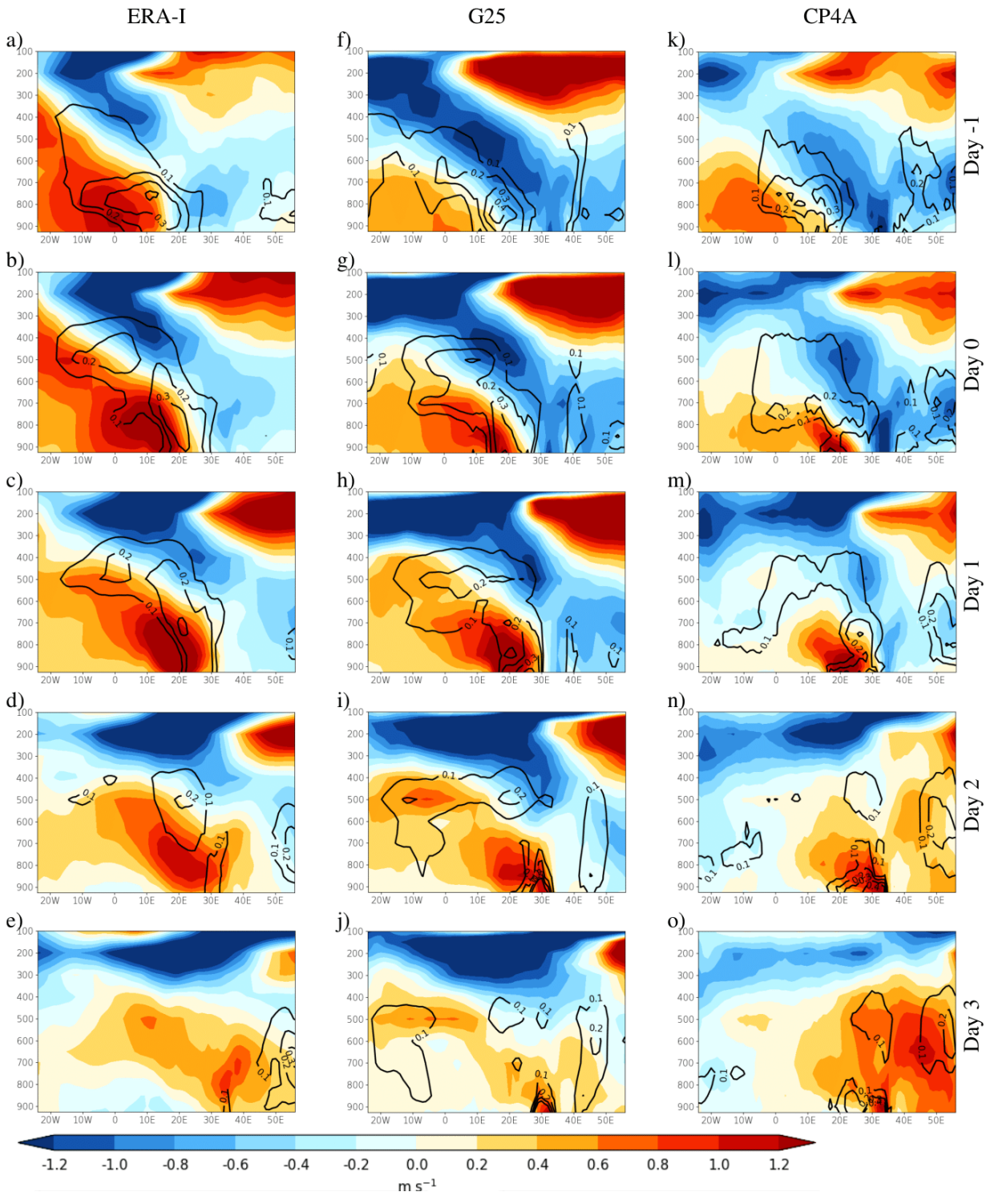

FIG. 5. Lagged height-longitude high-amplitude Kelvin wave event composite for anomalous zonal wind (shaded) and specific humidity (black contours) for (a-e) TRMM and ERA-I, (f-j) G25 and (k-o) CP4A. The lags for which a composite was computed are shown on the right of each row. Both fields are latitudinally averaged over 7°S-7°N. Specific humidity contour interval is 1.0 x 10^{-4}kg kg^{-1}. Only the positive specific humidity contours are shown.

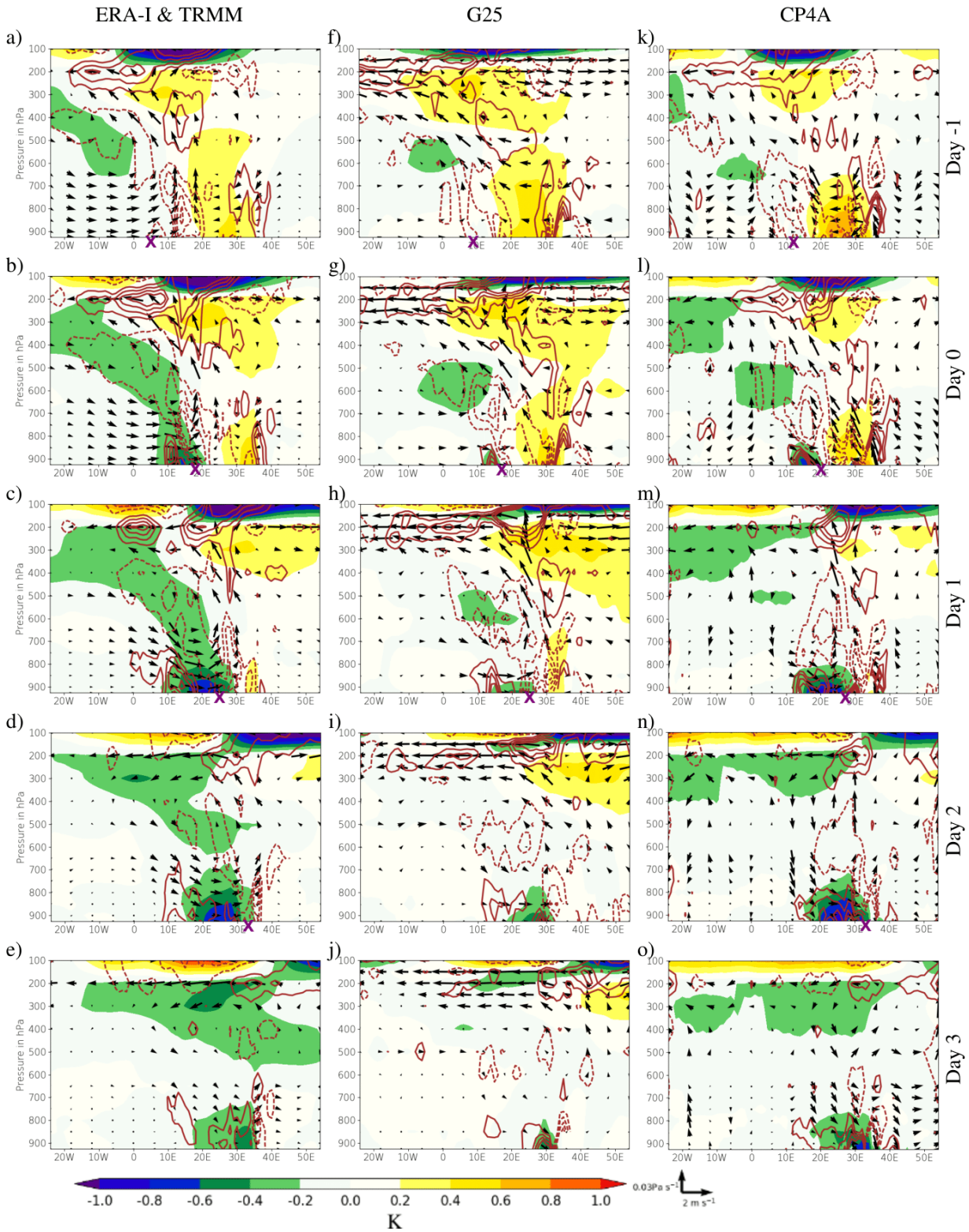

FIG. 6. Lagged height-longitude plots for (a-e) TRMM and ERA-I, (f-j) G25 and (k-o) CP4A showing high-amplitude Kelvin wave event composite for anomalous horizontal mass convergence (brown contours), potential temperature anomalies (shading) and anomalous zonal-vertical wind (vectors). The lag for which a composite was computed is shown on the right of each row. All fields are latitudinally averaged over 7°S-7°N. Vertical